https://doi.org/10.5194/egusphere-2022-842
Preprint. Discussion started: 12 September 2022

Directional Surface Wave Spectra And Sea Ice Structure from ICEsat-2 Altimetry

Momme C. Hell[1] and Christopher Horvat[1,2]

[1]Brown University, Providence, RI, USA

[2]University of Auckland, Auckland, NZ

Correspondence: Momme Hell (mhell@brown.edu)

Abstract. Sea ice plays an important role in Earth's energy budget by impacting surface albedo and air-sea fluxes in polar regions. On its margins, sea ice is heavily impacted by waves and we currently do not have routine observations of waves in sea ice and lack understanding of how waves interact with sea ice and how they attenuate.

In this paper, we propose methods to separate the two-dimensional (2D) surface wave spectra from sea ice height observations along each ICESat-2 track. A combination of a linear inverse method, called Generalized Fourier Transform (GFT), to estimate the wave spectra along each beam and a Metropolitan Hasting algorithm to estimate the dominant wave's incident angle was developed. It allows us to estimate the 2D wave signal and its uncertainty from the high-density, unstructured ATL03 ICESat-2 photon retrievals. The GFT is applied to re-binned photon retrials on 25 km segments for all six beams and outperforms a discrete Fourier transform in accuracy while having fewer constraints on the data structure.

The Metropolitan Hasting algorithm infers the wave direction from beam pairs every 25 km using coherent crests of the most energetic waves. Both methods together allow a decomposition into a 2D surface wave spectra with the advantage that the residual surface heights can potentially be attributed to other sea ice properties. The described method can routinely decompose ICESat-2 tracks and constrain wave attenuation in sea ice.

1 Introduction and Problem Description

Sea ice covers up to 9% of the world's oceans, and plays an important role in the energy balance of Earth's climate. Even though sea ice damps ocean surface waves (Squire, 2007), broad regions along the periphery of the sea-ice-covered ocean are continually under the influence of surface waves (Rapley, 1984; Horvat et al., 2020; Thomson, 2022; Horvat, 2022). These regions are collectively referred to as the Marginal Ice Zone (MIZ). In the MIZ, waves influence the thermodynamic and dynamic properties of sea ice, and also impact the coupled exchange between atmosphere and ocean. Currently we do not have a reliable global observations of waves in sea ice, and hence are unable to sufficiently understand air-sea exchange and wave

https://doi.org/10.5194/egusphere-2022-842
Preprint. Discussion started: 12 September 2022

propagation in the MIZ. This paper describes how ICESat-2 altimeter observations can be used to record waves spectra in the MIZ, and to infer additional sea ice properties to inform parametrizations of wave attenuation in sea ice.

Models of wave propagation in sea ice typically evolve the ocean surface wave spectrum, $\tilde{S}_h(k)$ (meter^2 k^{-1}, k is the wavenumber), which is attenuated when it comes into contact with sea ice. There has been significant debate over the functional form and dependencies of this attenuation (Squire, 2018; Thomson et al., 2021). Yet as it controls how deep waves reach into sea ice, it is vital for modeling MIZ variability and coupled feedbacks in the polar seas.

Constraining ice-induced wave attenuation is challenging because wave observations in ice are difficult to make at scale. A majority of observations of waves in ice are carried out using ships or arrays of floating buoys deployed by ships (or by helicopters from ships, see, for example Thomson, 2022, and references therein). While such observations provide high temporal frequency observations of wave spectra, they only cover a limited geographic domain, and are limited by the sea ice types and conditions at the original buoy locations. Recently satellite remote sensing technologies have shown promise for describing wave spectra in sea ice regions. SAR imagery is capable of observing wave crests as they move into the MIZ, and the two-dimensional wave spectrum can be constructed in good agreement with in-situ-observed spectra if the sea ice is not rough (Stopa et al., 2018; Ardhuin et al., 2017). However, SAR alone cannot observe continuous spectra as they propagate into the sea ice.

The ICESat-2 (IS2) altimeter has the potential for greatly increasing the available observations of wave-ice interactions, either alone, or in combination with other remote sensing instruments (Collard et al., 2022). ICESat-2 carries a single measurement tool, ATLAS, a six-beam laser oriented in three weak/strong pairs (Fig. 1a, colored lines) offset at a near-uniform three kilometers on the ground, with a weak-strong beam lateral offset of about 90m meters. ATLAS measures the return time of individual photons to infer the height of the ice/ocean surface. Typical along-track photon spacings can be centimeters or smaller, and so IS-2 is capable of directly sampling ocean surface waves, particularly over reflective sea ice.

Recent studies have examined waves in sea ice using IS-2, basing their results on a higher-order sea ice height product derived from photon retrievals (known as ATL07). Horvat et al. (2020) identified the capability of IS-2 to retrieve ocean waves by examining a storm in the Barents Sea in 2019, and used a simple threshold to establish where and when waves were observed in the sea ice to produce global maps of the MIZ. In Collard et al. (2022), IS-2 retrievals during this Barents Sea storm were shown to compare well with model and SAR-based observation data. Brouwer et al. (2021) selected a series of Southern Hemisphere IS-2 retrievals, analyzing wave attenuation using direct spectral transform methods. Both found that areas affected by waves were common in both hemispheres, with repeated measurements of waves hundreds of kilometers into the sea ice zone, particularly in the Southern Hemisphere.

Three challenges limit the direct comparison of IS-2 derived wave spectra to observations and models. First, waves propagate at an angle θ relative to the along-track direction of the satellite (Fig. 1b), and observable wave lengths λ are aliased by an unknown factor $\cos^{-1}\theta$ (Rapley, 1984; Horvat et al., 2016; Yu et al., 2021). Second, observed surface height variability is a convolution of the dynamic ocean topography, sea ice topography, surface waves, and noise. The surface wave signal can than only successfully reconstructed if these other signals are on a different scale, like the ocean topography, or not periodic, like the sea ice topography and noise. Third, the fractured nature of sea ice, influence of clouds, and changing surface albedo cause

https://doi.org/10.5194/egusphere-2022-842
Preprint. Discussion started: 12 September 2022

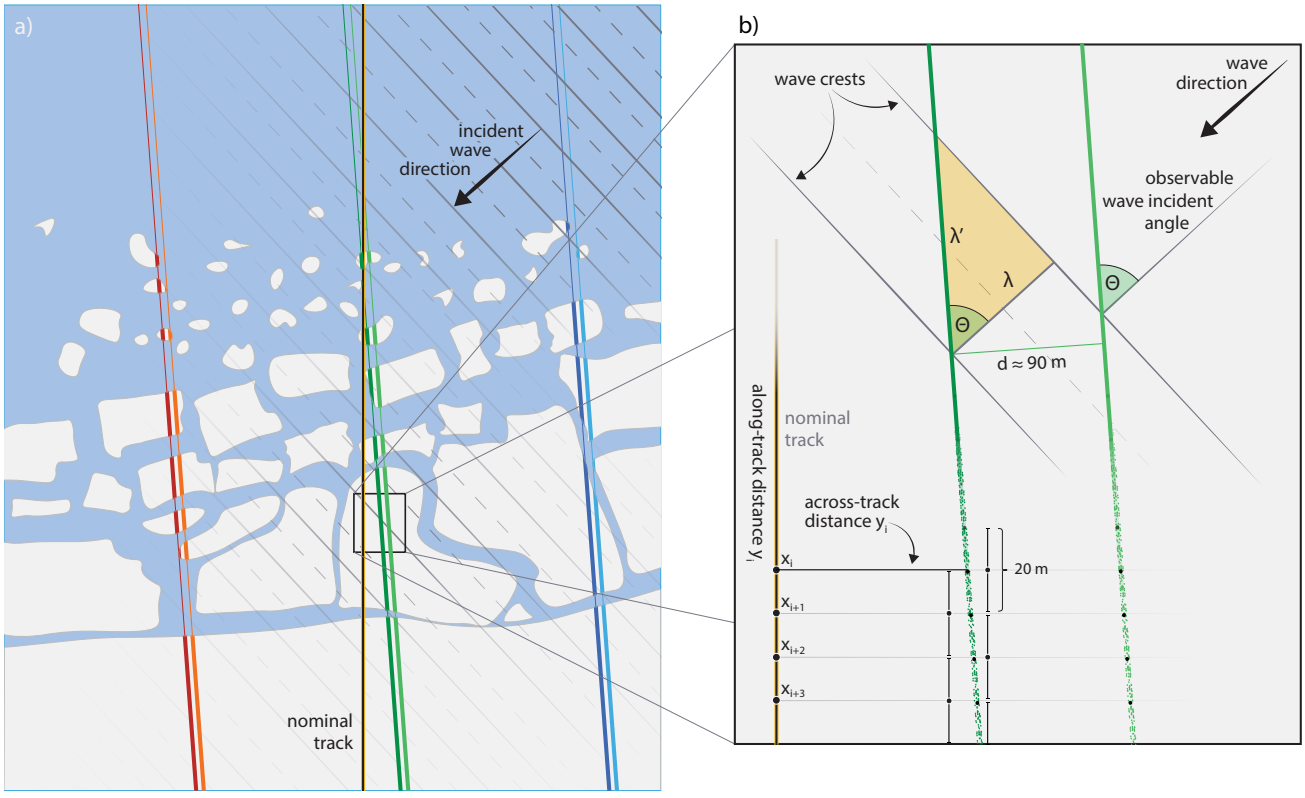

Figure 1. Illustration of ICESat-2 (IS2) beams intersecting the Marginal Ice Zone (MIZ) under the presence of waves. a) The three beam pairs are shown is red/orange, dark/light green, or dark/light blue lines. The vertical black line is the nominal IS2 reference ground track. The incident waves come from the top-right along the black arrow with wave crests (solid) and valleys (dashed). b) Details view of an ideal monochromatic wave observation by IS2 in sea ice. The IS2 beam pair (light/dark green lines) observes an incident wave (along the black arrow) of wavelength λ with an angle θ as λ'. With the beam-pair distance d one can calculate θ from the phase lag of the incident wave crests. The along-/across-track coordinate system is referenced to the nominal track, while each data point is the weighted mean a 20-meter stencil (see text).

gaps or irregularities in IS-2 photon retrieval rates, creating an high-density but irregular observation. The method must be applicable to irregular data without generating spurious sources of variance, i.e. artificial wave energy. All of the above factors complicate direct assessments of spectra and their attenuation in sea ice.

Here we develop angle-corrected, two-dimensional (2D) wave spectra in sea ice, using photon height data from ICESat-2. We partition surface height variability into waves and sea-ice or noise-related components, which permits a direct assessment of wave energy attenuation and sea-ice properties for evaluation of numerical attenuation schemes. We show this partitioning allows for significantly improved sea ice height estimates in the MIZ, which may allow for an expansion of existing higher-level IS-2 products to broader ice-covered regions.

We describe the pre-processing of IS-2 along-track photon heights in section 2.1 and develop a (linear) harmonic fitting procedure applied individual IS-2 beams in section 2.2. Subsequently we develop a multi-beam, Monte-Carlo method for bias-correcting along-track wavelengths in section 3. We then demonstrate this method on three example cases (Track 1 to 3, see

https://doi.org/10.5194/egusphere-2022-842
Preprint. Discussion started: 12 September 2022

suppl. Table for granule names), providing two-dimensional wave spectra derived from along-track data in section 3.2, and the decomposition of photon variance in section 4. In section 5 we address how the angle correction and variance decomposition can be used to both (a) developed improved models of attenuation of waves in sea ice, and (b) improve estimates of sea-ice freeboard.

2 Along-track Wave Spectra from IS-2

The primary aim of this analysis is to assess surface height variability in the MIZ. Hence we want to use the highest data resolution we can handle, though we are agnostic about the classification of photon returns. That is the L2-level product ATL03 from Neumann et al. (2021). For comparison, we show the photon cloud data from ATL03 and the surface heights and type classifications from the higher level ATL07/10 product in figure 2 as dark blue, light blue, or orange dots (Kwok et al., 2021). By requiring 150 consecutive photons to identify a sea ice segment, the ATL07 product accounts for most of the height variability from the ATL03 product. Yet it misses retrievals in the MIZ (supl. Fig. 2, white and gray area) and within the sea ice (Fig. 2). For better resolution, the following analysis is based on the photon cloud data from ATL03.

2.1 Data Pre-Processing

Linearly inverting photon data requires exact along and across-track information about photon positions. Along-track photon positions are first re-referenced to the most equatorward position on the nominal ATLAS ground track. The most equatorward position is evaluated from the ATL07 (Kwok et al., 2021) product and set to the beginning of 1st 100 km section that has at least 0.02 photons per 100km. All tracks are then followed in a poleward direction, until the variance of any of the 6 beams exceeds a factor of 10 the variance of the first 15% on the equatorward side of the track (supl. Fig. 2, dashed black lines). This avoids including impacts from coastal or land ice around the Antarctic coast. The redefined along-track direction x and an across-track direction y are then used as coordinate system throughout the analysis (Fig. 1b, supl. Fig. 1 and 2).

After removing the cumulative surface height correction (`dem_h` taken from the ATL07/10 dataset, Kwok et al., 2021), we bin photon measurements into 20-meter stencils that overlap by 50%. This yields a 10-meter along-track resolution (Fig. 2 green line). Note this differs from the procedure used to form sea ice surface heights in the ATL07 product, which averages height data for each set of 150 photons along-track. ATL07 has a constant photon count, with the trade-off of irregularly spaced segments of varying length in the MIZ, while our approach provides more regularly-spaced data with the trade-off of having a variable photon count in each stencil and potentially including retrievals of water near sea ice. Stencils with fewer than five photons are excluded, which also leads to data gaps corresponding to no or very low photon retrievals due to sea-ice leads, open water, clouds, or other noise (suppl. Fig. S2). These data gaps also lead to an irregularity in the data, but here each stencil mean represents the same area and hence better capture wave phase.

The photon height in each 20-meter stencil $h_c(x)$ is calculated as the mean of the photons weighted by their inverse distance to the stencil center, using a Gaussian weighting function with standard deviation of 10m. We tested other data reduction methods, like using the median or mode of the stencil, finding results insensitive to the choice of the binning method (suppl.

https://doi.org/10.5194/egusphere-2022-842
Preprint. Discussion started: 12 September 2022

Fig. S2). The same 20-meter stencil also provides an uncertainty estimate $\sigma_h(x)$ (proportional to Fig. 2 blue area) representing the varying photon density. This uncertainty is used to define the data prior (sec. A1) for the harmonic inversion in section 2.2.

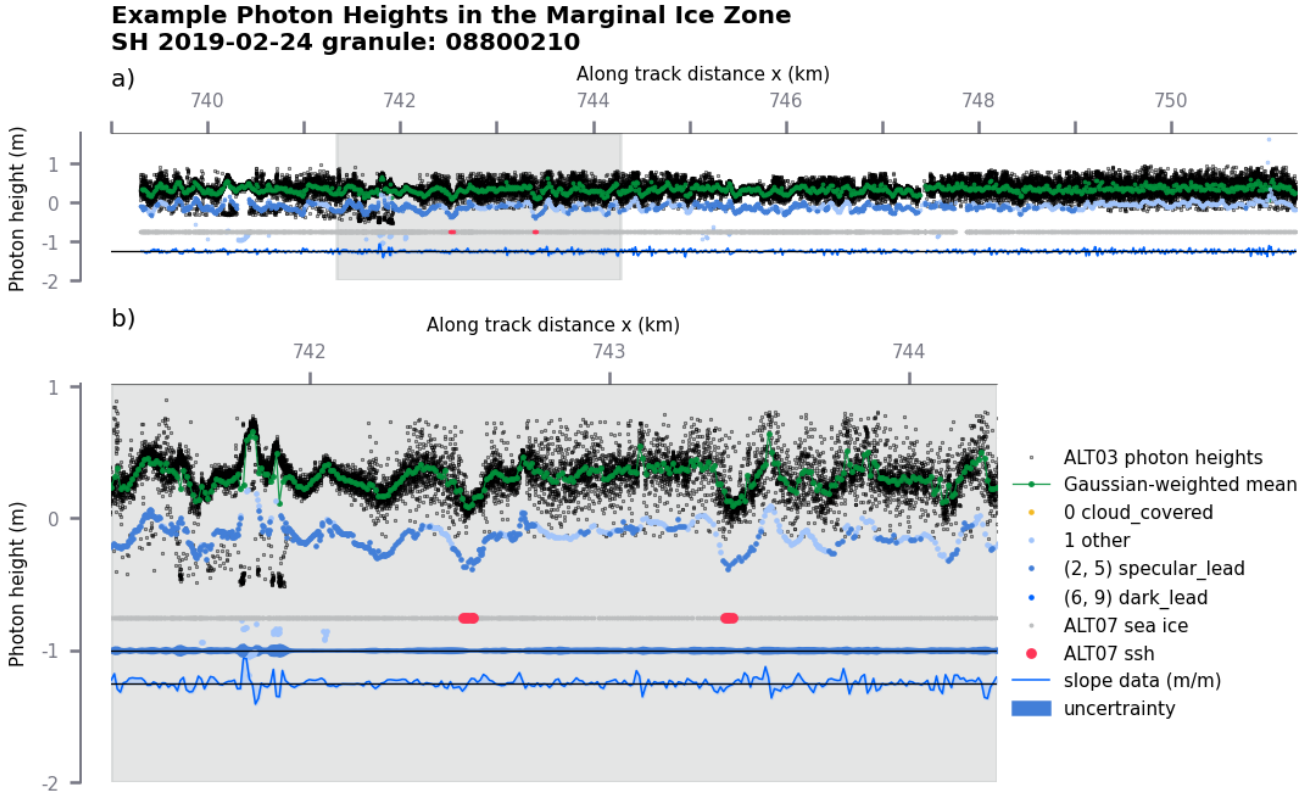

Figure 2. ATL03 photon cloud and ATL07 surface heights for example Track 1. Individual photons are shown in black and the 20-meter weighted average as a green line. The ATL07 Photon heights are are shown as light blue, dark blue, or black dots, with the color corresponds to their type category provided in ATL07. Identified sea ice leads are shown as red segments on the gray line. The surface slope based on the weighted photon average is shown as a blue line with -1.25 offset, and its uncertainty estimate as blue shading with a -1 offset. The panel b) is an inset of the gray area in panel a).

The re-sampled surface height data is used to calculate a series of along-track surface slopes (Fig. 2 thin blue line) by taking the along-track derivative and applying a spike-removing algorithm. Using the along-track surface slope data focuses the timeseries analysis on local photon-height changes, rather then the magnitude of the total surface height field. The spike-removal reduces peaks in the slope data, which can be from sea-ice height changes or especially those resulting from ice-ocean transitions. Because the slope field approximates the derivative of the height field, the spectrum of slopes $\hat{S}_c(k)$ is readily connected to the spectrum of surface heights $\tilde{S}_c(k)$, as $\tilde{S}_h(k) = k\tilde{S}_c(k)$. The surface height field can therefore be directly reconstructed from the slope spectrum, as we show below. The generalized Fourier transform (sec. 2.2) and directional estimates (sec. 3.1) are then applied on 25-km long segments of these surface slopes, with uncertainty estimates (Fig. 2). The 25-km segments also overlap by 50%, providing an along-track spectral estimate every 12.5 km.

https://doi.org/10.5194/egusphere-2022-842
Preprint. Discussion started: 12 September 2022

2.2 Generalized Fourier Transform (GFT)

We estimate along-track wave spectra using a Generalized Fourier Transform (GFT). The GFT is an harmonic fit of sin- and cos-pair coefficients, which together determine amplitude and phase at each wavenumber. The model complexity is defined by the number of resolved wave numbers and its success depends on prior (assumed) knowledge about the data's uncertainty and model structure.

We use a GFT to overcome several disadvantages arising when implementing a standard Discrete Fourier Transform (DFT). While the DFT is a fast variance-conserving algorithm it requires periodic, continuous and equally-spaced data. The DFT implies that frequency bands are harmonics over a domain or segment length L, which is an arbitrary limitation on the resolved frequencies. To make segments periodic, often tapering or windowing is applied to the segmented data. In addition to the data's non-periodicity the common presence of data gaps in IS-2 retrievals requires extrapolation or gap-filling to create continuous equally spaced data suitable for a DFT. These both lead to commonly known problems of the DFT, like energy leaks/compensation in spectral space. The data handling needed for DFT can erode the signal substantially, especially in the MIZ (Fig. 3 b,c gray and green lines).

The GFT method outlined below works on any grid, incorporates data uncertainty, and does not require periodicity. The GFT can be customized to the frequencies of interest with the additional benefit of providing a standard error in real and wavenumber space.

2.3 Harmonic wave inversion

We follow Wunsch (1996), Menke (2018), and Kachelein et al. (2022), using generalized least squares to derive spectral amplitudes in each 25-km segment X_i (Fig. 4). Slope data in each section X_i is a series of unevenly spaced mean-zero data points and is expressed as a column vector $\mathbf{b} = \partial_x \mathbf{z}$ of length N_i where $\mathbf{z}$ are the height data. These data are then modeled as the sum of sinusoids having wave numbers in the range of swell and wind waves

$$\mathbf{b} = \mathbf{H}\,\mathbf{p} + \mathbf{r}, \tag{1}$$

where $\mathbf{H}$ is an $N_i \times 2M$ regressor matrix of basis functions, $\mathbf{p}$ is the model parameter vector of length $2M$, and $\mathbf{r}$ is the vector of the residual timeseries of length N_i. The columns of $\mathbf{H}$ are sines and cosines of prescribed wave numbers, $k_m = 2\pi/\lambda_m$ for wavelengths λ_m indexed by $m = 1, 2, ..M$, i.e.:

$$\mathbf{b} = \sum_{m=1}^{M} \Big(a_m \cos(k_m \mathbf{x}) + b_m \sin(k_m \mathbf{x}) \Big) + \mathbf{r}, \tag{2}$$

$$\tag{3}$$

https://doi.org/10.5194/egusphere-2022-842
Preprint. Discussion started: 12 September 2022

with,

$$\mathbf{p} = [a_1, a_2, ...a_M, b_1, ...b_M]^T \tag{4}$$

$$\mathbf{x} = [x_1, x_2, ..., x_{N_i}]^T. \tag{5}$$

To find the most probable $\mathbf{b}$ given a set of model parameters $\mathbf{p}$, we need to estimate the autocovariance matrices of the residual $\mathbf{R} = \langle \mathbf{r}\mathbf{r}^T \rangle$, i.e. the error of the data, and the autocovariance matrix of the model $\mathbf{P} = \langle \mathbf{p}\mathbf{p}^T \rangle$, where $(\langle \cdot \rangle)$ is the expected value. Then the most probable estimate of the data $\mathbf{b}$ can be found by estimating the maximum of the posterior probability distribution $P(\mathbf{p}|\mathbf{b})$. Using Bayes' theorem (Kachelein et al., 2022), or, alternatively the matrix inversion lemma (Wunsch, 1996), given the data $|\mathbf{b}$, the most likely estimate of the model parameters $\hat{\mathbf{p}}$ is found as,

$$\hat{\mathbf{p}} = \left(\mathbf{H}^T\mathbf{R}\mathbf{H} + \mathbf{P}^{-1}\right)^{-1} \mathbf{H}^T\mathbf{R}^{-1}\mathbf{b}. \tag{6}$$

Once the model parameters $\hat{\mathbf{p}}$ are estimated, the model can be expressed in real space using $\hat{\mathbf{b}}$ (Fig. 3a green lines), or as a power spectrum $\hat{\tilde{\mathbf{S}}}_{GFT}$ (Fig. 3b,c green lines, see suppl. material S1 for derivation). Note that $\hat{\tilde{\mathbf{S}}}_{GFT}$ is substantially different from that of the DFT of the same data (Fig. 3b,c gray and green lines respectively). The frequent gaps in the data, as well as the DFT's requirement for the data to be period creates artificial power in the swell's wavenumber range that lead to miss leading results.

To estimate the model error, the posterior autocovariance of the difference between estimated and true model parameters is defined as the inverse Hessian,

$$\mathbf{Hess}^{-1} = \langle (\mathbf{p} - \hat{\mathbf{p}})(\mathbf{p} - \hat{\mathbf{p}})^T \rangle = \left(\mathbf{H}^T\mathbf{R}\mathbf{H} + \mathbf{P}^{-1}\right)^{-1}, \tag{7}$$

In practice this is calculated from the so called "kernel" matrix $\mathbf{H}$, and the (assumed) Gaussian distributed data and model priors $\mathbf{R}$ and $\mathbf{P}$. The inverse Hessian is then be used to estimate the error of the model parameters

$$\hat{\mathbf{p}}_{err} = \mathrm{tr}(\mathbf{Hess}^{-1}), \tag{8}$$

(Fig. 3d, shown in the same units as the power spectra) and the error of the fit to the modeled data,

$$\hat{\mathbf{b}}_{err} = (\mathbf{H}^2\ \mathbf{Hess}^{-1})\mathbf{j}, \tag{9}$$

(not shown) where $\mathbf{j}$ is a unit vector of length $2M$.

https://doi.org/10.5194/egusphere-2022-842
Preprint. Discussion started: 12 September 2022

2.3.1 Choice of model resolution and degrees of freedom

The quality of the GFT model depends on the degrees of freedom, the model prior $\mathbf{p}$, and data priors $\mathbf{r}$ (eq. 7). While the number of model parameters, $2M$, remains fixed throughout the analysis, the number of data points in segment i, N_i, is variable, and may be controlled by the segment length L, 25 km in our case, with a 12.5km overlap (Fig. 4).

The number of degrees of freedom is then $2M - N_i$ and depends on the number of data points in each 25-km segment. A segment with no data gaps and a 10-meter resolution (sec. 2.1) contains $N_i = 2500$ data points. With $2M = 1738$ model parameters, this is then an over determined problem. However, frequent data gaps reduce the number of datapoint per segment, which may result in an underdetermined problem, with more model parameters then data ($2M > N_i$). The result is then a larger residual $\mathbf{r}$ and larger uncertainty estimate $\hat{\mathbf{p}}_{err}$ (eq. 8 and eq. 9). Even in cases where eq. (1) is underdetermined, we are confident in our wave spectrum estimation within given error because $\mathbf{P}$ contains prior knowledge about the shape of the solution, i.e. the shape of typical surface wave spectra (sec. 2.4).

The choice of segment length also determines the smallest resolvable wavenumber. For example, a segment length of 25-km resolves a wave with a 20s period at an incident angle of $\pm 75°$ about 10 times. We set the lowest resolved wavenumber to $k_1' = 2.5 \times 10^{-3}$ rad m^{-1} which corresponds to a maximum wavelength of 2500 meters (sec. 3.1). The highest wavenumber is chosen as $k_m' = 0.11$ rad m^{-1}, a typical period of wind waves of about six seconds. Using evenly spaced wavenumbers with $dk = 1.25 \times 10^{-4}$ this results in $M = 869$ wavenumbers.

2.4 Iterative inversion along each beam

The GFT solution $\hat{\mathbf{b}}$ depends on prior assumptions about the wave spectrum: the model prior $\mathbf{P}$. Since the GFT is iteratively applied along each beam, results from a previous (closer to the open ocean) segment inform the subsequent segment as illustrated in Figure 4. Here we describe how a successive application of the GFT along the IS-2 beam can leads to an efficient solution assuming that the wave's spectral shape only slowly varies between the segments.

The initial guess of the model prior $\mathbf{P}_{init}$, taken at the most ocean-ward edge of the data is a Pierson-Moskowitz (PM) spectral slope function (based on Pierson and Moskowitz, 1964), to describe the general shape of a narrow banded surface wave field. The initial PM form is fit to a DFT of the data, and any locations with missing data are defined with a slope of zero. This gap-filling creates artificial ringing in the DFT, but is sufficient to estimate the peak wave number and energy of the spectrum. The PM-spectrum has, in its simplest form only two free parameters, the peak frequency and spectral amplitude, which are fit to the DFT power spectra via an objective function that is regularized by the observed spectral peak of the smoothed data (Appendix A, Hell et al., 2019).

The initial inversion of the most equatorward segment X_0 is performed using $\mathbf{P}_0 = \mathbf{P}_{init}$ in eq. (6), leading to model parameters $\hat{\mathbf{p}}_\mathbf{0}$. For this first segment, a second inversion is applied on the same data, using an updated prior that is a smoothed version of $\hat{\mathbf{p}}_\mathbf{0}$ (Fig. 4, left). The smoothing uses a Lanzos running smoother in wavenumber with a stencil-width of ± 0.19 2πm^{-1}, or 150 data points. Inversions of the successive segments $X_1, X_2, X_3, ...$ are then performed once, with the prior $\mathbf{P_i}$

https://doi.org/10.5194/egusphere-2022-842
Preprint. Discussion started: 12 September 2022

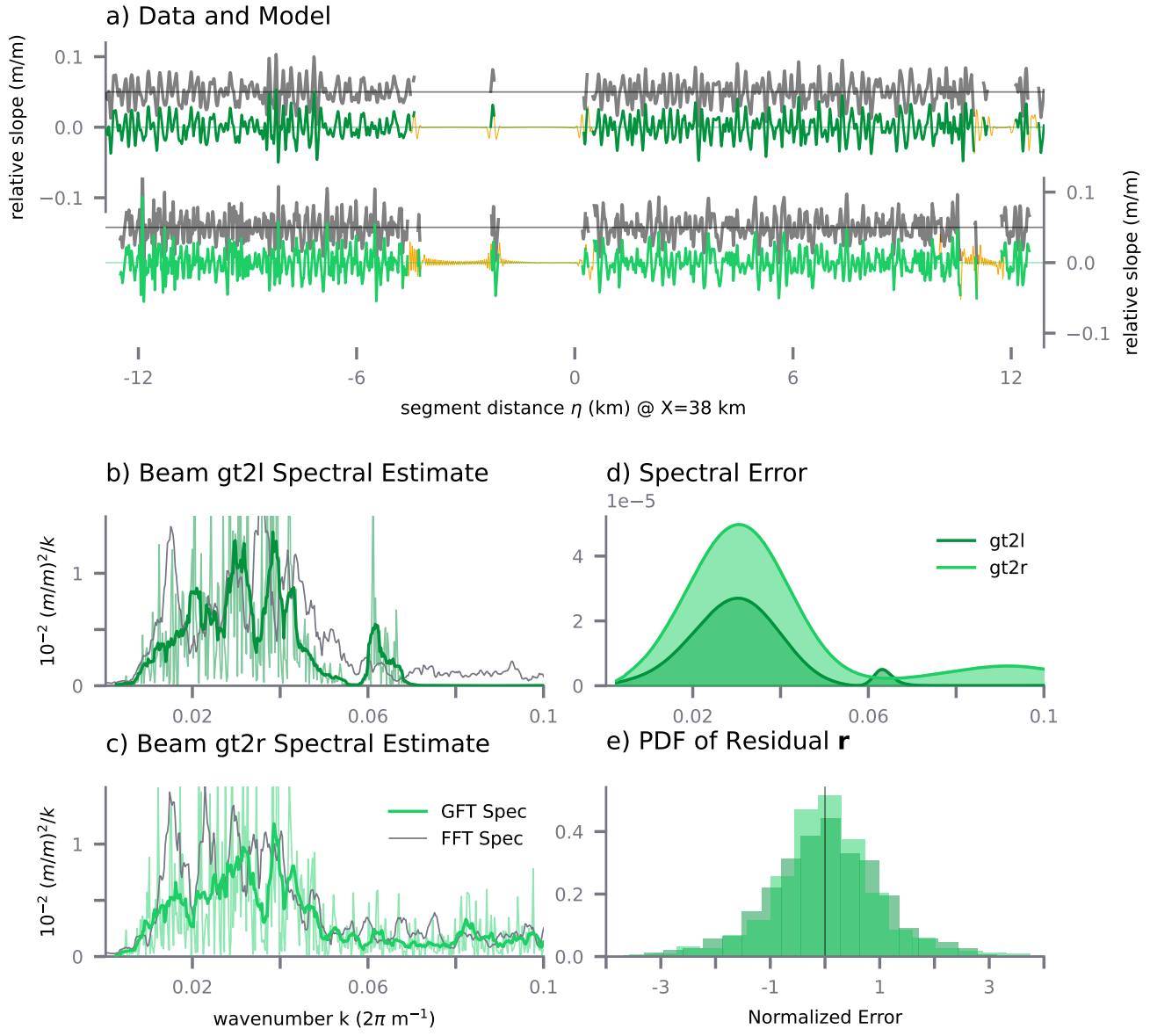

Figure 3. Example model and spectral estimate for a 25-km segment in the MIZ for Track 2 (granule `08070210`, see suppl. Table). (a) Data (gray), model (dark and light green), and predicted modeled (orange) photon heights for two neighboring beams gt2l (dark green) and gt2r (light green). The data is offset by 0.5. (b and c) Corresponding power spectral estimates using GFT (green) and standard DFT (gray). The thick green lines are smoothed GFT estimates with a rolling 10-wavenumber mean. (d) Power spectral error for both beams as function of wave number. e) Residual PDF of **r** for both beams respectively.

a smoothed version of $\hat{\mathbf{p}}_{i-1}$. If missing data does not allow for a successful inversion, the algorithm is re-initiated as done to obtain $\mathbf{P}_0$ and $\hat{\mathbf{p}}_\mathbf{0}$.

https://doi.org/10.5194/egusphere-2022-842
Preprint. Discussion started: 12 September 2022

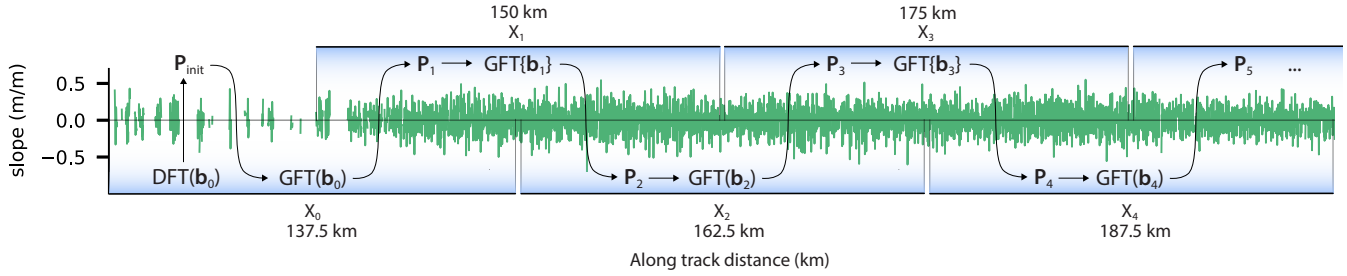

Figure 4. Schematic of the harmonic inversion algorithm along an ICESat-2 beam, shown over the surface slope field of a typical beam in the MIZ. The DFT in each successive segment X_i has a prior $\mathbf{P}_i$ derived from the previous segment centered around X_{i-1}. For those segments with no prior information available, the prior $\mathbf{P}_{init}$ is generated via a Discrete Fourier Transform (DFT) over the segments centered at X_i.

2.5 Tracking of wave energy through Sea Ice

The GFT is applied to each 25 km-segment with more then 250 data points, leading to wave spectral estimates along each beam. In Fig. 5(a-f) we show wavenumber spectra for each segment and for each of beams of Track 3 in the Southern Hemisphere on May 2, 2019. The per-segment cross-beam mean (Fig. 5h) and mean spectral error (Fig. 5i) are derived by weighting each segment by its photon density before taking the mean. We define this weighted mean and error as our best estimate of the along track spectral evolution of wave energy.

The example track shows an attenuating swell signal starting at $X = 0$ km and a second wave-energy maximum with shorter wavelength ($k' \approx 100m$) at about $X = 150$ km in both, the spectrogram of the weighted mean as well as in individual beams (Fig. 5a to f, and h). The corresponding error per wave-number and position indicates larger error were we see wave signals (Fig. 5 i) which are likely just related to larger amplitudes in the data.

The estimated wave numbers are the observed along-track wave numbers k', which are different than the true wave number length $|\mathbf{k}|$ along the incident wave vector $\mathbf{k}$ (see Fig. 1). To estimate a wavenumber spectrum along the dominant propagation direction rather then the direction it is observed, we outline a method to correct this bias in the following section.

3 Two-dimensional wave spectra from nearly one-directional observations

3.1 Metropolitan estimates of the incident angle

The observed wave spectra are distorted by a misalignment between the wave's incident angle and the beam's direction (Fig. 1b). While the ICESat-2 track orientations are well known, the surface waves can originate from any direction, and the angle between these two directions is θ. If θ is known, the observed wave number k', or wavelength λ' along the beam can be corrected using $k = k' cos^{-1}(\theta)$. The same geometrical distortion will also affect estimates of the attenuation rate between X_i-positions along the track (Fig. 1b) because the wave energy attenuates along their dominant propagation direction and not along the direction they are observed by the satellite.

https://doi.org/10.5194/egusphere-2022-842
Preprint. Discussion started: 12 September 2022

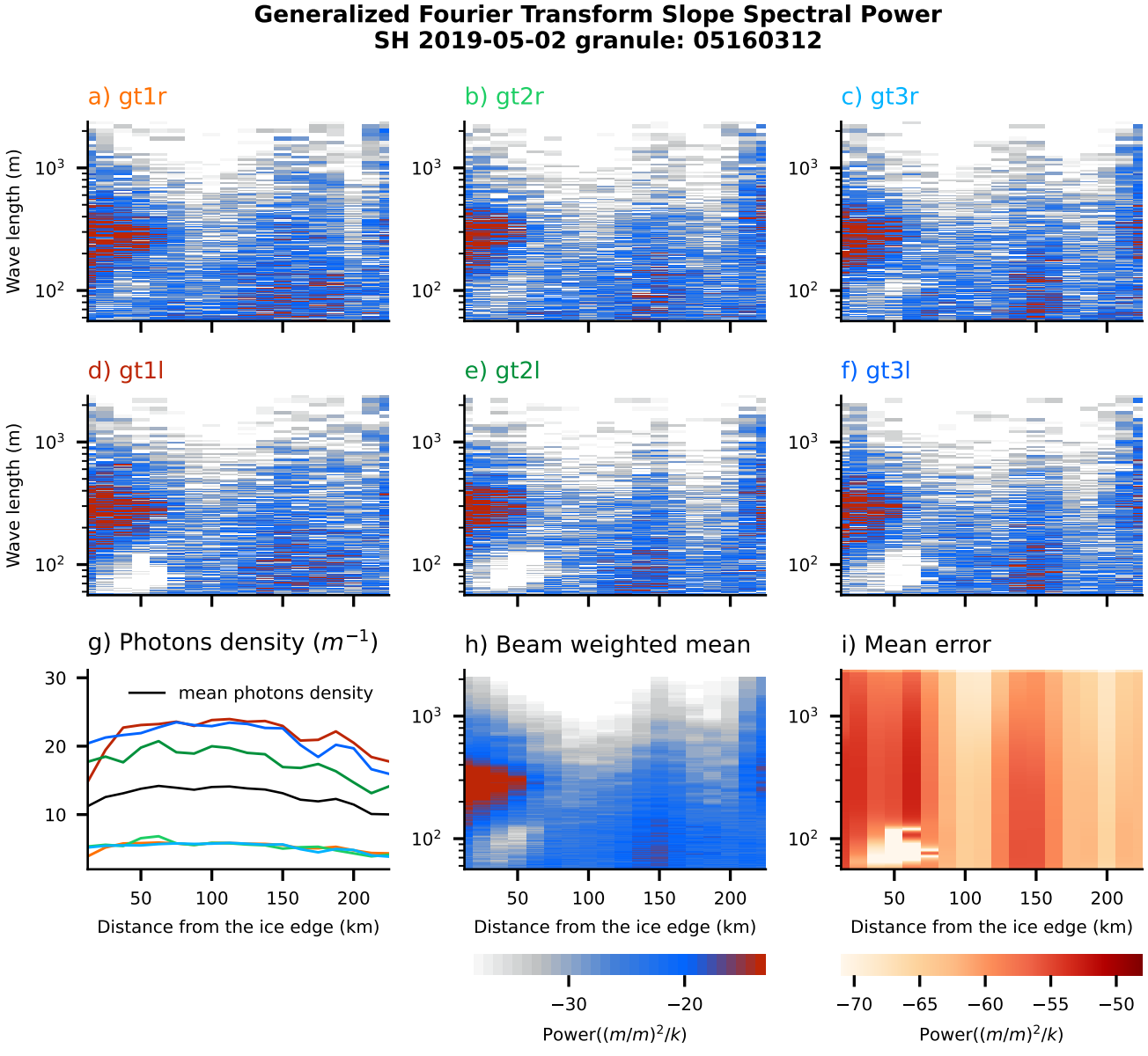

Figure 5. Slope spectra for the six beams (a to f) of example Track 3 (granule `05160312`, see suppl. Table) resulting from the GFT inversion (sec. 2.4) for granule 05160312. The photon density per segment (g) is used to calculate the weighted mean spectrum (h) and error (i) for each track segment.

215 To estimate θ from the photon data we make use of the spatial coherence between weak-strong beam pairs. That means wave crests observed in one beam may also be observed in the other. Yet using the coherence has several limitations that have to be taken into account when designing an optimization method:

https://doi.org/10.5194/egusphere-2022-842
Preprint. Discussion started: 12 September 2022

- The coherence between beam pairs can only usefully be calculated for not too oblique angles (about $\pm XX°$, Suppl. Fig. S3, and Yu et al., 2021) and high enough photon densities in both beams.

- Across-beam coherence relies on an accurate measure of the distance the beams. Uncertainty in the intra-beam distance d can further obscured angle estimates based on coherence (Fig. 1b). Since d varies along the track (suppl. Fig. S1), using the nominal distance rather then the observed value will bias angle estimates.

- The complex generation and propagation history of waves (Kitaigorodskii, 1962; Villas Bôas and Young, 2020; Marechal and Ardhuin, 2021; Hell et al., 2021a) leads to a dynamic distortion in the incident angle. While a monochromatic plane wave would be coherent across beam pairs, estimating its direction is limited by the periodicity of the waves and observational noise. In reality, the incident swell wave energy at any given time is contained in several wavenumbers although concentrated in a narrow-banded 2D-spectrum (Longuet-Higgins and Deacon, 1957). Hence, the bandwidth of the 2D swell field limits the coherence between strong/weak beam pairs. While a narrower 2D-spectrum results in coherent wave crests in the across wave-direction, a broader spectrum spans more random-phase waves, which diminishes the coherence between wave crests (suppl. Fig. 8). Less wave-crest coherence in broader spectra limits estimates of the incident angle when the surface is only observed along two beams.

With IS-2, the incident wave energy along $\mathbf{k}$ is observed along the beam direction for wavenumbers $k' = |\mathbf{k}| \cos^{-1}\theta$, or as a distorted wavenumber because of the above described distortion. In the case of IS-2 beam pairs, we know neither θ nor the bandwidth of the incident spectrum (Longuet-Higgins, 1984) and both factors limit the angle inversion based on beam pairs alone (suppl. Fig. S8). Despite these limitations, we describe in the following how the incidence angle θ can still be retrieved within these limitations.

As explained in section 2.2, the surface wave field can be interpreted as the superposition of monochromatic plain waves. For a narrow-banded swell spectrum the majority of the wave energy is contained in a few wave numbers and hence a superposition of the most energetic monochromatic waves explains the majority of the surface slope variability. In the following we optimize the incident angle and phase of the most energetic monochromatic waves numbers using a Metropolis-Hastings algorithm (Foreman-Mackey et al., 2013). We accumulate the marginal distributions of possible incident angles across the dominant wave numbers and beam pairs, which results in a best guess of possible incident angle. This approach leads to directional wave information similar to the maximum entropy method used in wave buoys (Lygre and Krogstad, 1986).

We focus on the 25 most-energetic wavenumbers of each beam pair and segment X_i based on the GFT result (sec. 2.2). To identify these wavenumbers, the beam-pairs mean wave power is smoothed using a three-wavenumber running mean to select possible wave-numbers within the distorted narrow-banded spectrum (similar to the thick green lines in Fig. 3 b,c). For each of these $n = 25$ observed wavenumbers k'_n, we define a monochromatic model,

$$\hat{\mathbf{h}}_n(\boldsymbol{\eta}, \boldsymbol{\nu} \,|k', \theta, \phi) = \cos(k'\boldsymbol{\eta} + l'\boldsymbol{\nu} + \phi), \tag{10}$$

https://doi.org/10.5194/egusphere-2022-842
Preprint. Discussion started: 12 September 2022

in the local reference system of the segment centered around X_i and $y = 0$ such that the local along-track coordinate is $\boldsymbol{\eta} = \mathbf{x} - X_i$ and the across-track coordinate is $\boldsymbol{\nu} = \mathbf{y}$ with the observable across-track wavenumber $l' = k' \tan(\theta)$, and the phase ϕ.

The monochromatic model is than used to define the objective function Φ_n for each wavenumber

$$\Phi_n = ||\mathbf{b} - \hat{\mathbf{h}}_n||^2 + \beta_\theta \; P_{\theta,n}(\theta), \tag{11}$$

where $\mathbf{b}$ is the normalized slope data of the beam pair, β_θ is a hyper-parameter which controls the regularization $P_{\theta,n}$ of the incidence angle θ for the n-th wavenumber, and $P_{\theta,n}(\theta, k)$ is a prior estimate that we describe in sec. 3.1.2.

The log-probability of the objective function eq. (11) is sampled for each beam pair, selected wavenumber, and along-track position X_i. To derive independent estimates of the incident angle for each n-th wavenumber we use an Metropolis-Hastings Scheme (Marcov-Chain Monte Carlo, MCMC, Foreman-Mackey et al., 2013) by first initializing equally-spaced samples of the objective function over the domain $\theta = [-0.47\pi, 0.47\pi]$ and $\phi = [0, 2\pi)$ and advancing the ensemble of samples (ensemble of walkers) using MCMC. The MCMC method will quickly cluster walkers in the areas of low-cost, or small objective function (Fig. 6b, black dots). A high density of walker positions is than interpreted as a high likelihood of an incident angle and phase for the chosen wavenumber (Fig. 6b, black dots).

We derive a sample of the joint phase and angle distribution by advancing the walkers 300 iterations, and only the last 270 iterations for each walker are used to established the joint histogram $D(\theta, \phi)$. The joint histogram D is then marginalized for the incident angle θ and normalized to a probability distribution function (Fig. 6c). This procedure is repeated for each selected wavenumber k_n and for each (available) beam pair per segment X_i (Fig. S9 a to c). The best incident angle PDF $\theta_{PDF}(X, k, beampair)$ can then be derived using the weighted average across wavenumber, beam-pair, or both.

The resulting beam- and wavenumber-average PDF of Track 3 at $X_i = 87$, for example, shows more than one maximum (Fig. 7b). (Here the individual PDFs are weighted by the mean power of the respective wavenumber and the number of data points per segment pair). This more complex marginal distribution comes from different maxima in PDFs of different wavenumbers. If one trusts the angle estimate of a single wavenumber, this can be interpret as a wave field with waves from multiple directions. The alternative – likely better – perspective is that the marginal PDF of each wavenumber is not a robust estimate the incident angle, and hence the PDF in figure 7b is the result of the uncertainty of the method, as explained in the next section.

3.1.1 Robustness of the Marginal PDFs

The described limitations in retrieving the incident angle (sec. 3.1) indicate a low signal-to-noise regime and demand a careful evaluation of the method for sampling the objective function Φ_n. While larger samples may ensure convergence of the distribution estimate, a large sampler of each wavenumber, beam pair, and segment may not be necessary, or computationally affordable. We decide for a systematic under-sampling of each realization of the marginal PDFs $\theta(X_i, k, beampair)$ and, in a second step, make a super-sample from the marginal PDFs across beam pairs and wavenumber if needed.

https://doi.org/10.5194/egusphere-2022-842
Preprint. Discussion started: 12 September 2022

When combining the systematic under-sampled PDFs they are still statistically robust. Each realization of the joint θ-ϕ distribution requires 6750 function evaluations for 270 iterations per walker. The walkers auto-correlation is about 20 to 30 iterations, which implies that each joint distribution maybe not be well established (the effective degrees of freedom per walker are about 9 to 14). Hence the marginalization of each joint distribution may misrepresent the angle uncertainty (i.e. a too wide distribution of the walker's PDF). To reduce uncertainty, we take a super-sample of marginal PDFs, by averaging across wavenumbers and/or the three beam pairs. The super-sampling results in a statistically robust result with 5×10^5 function evaluations per segment X_i, that is about effective $3.5 - 5.5 \times 10^3$ degrees of freedom per segment. Longer Markov Chains, i.e. more iterations, may result in a better sampling of the individual fit, but may not affect the overall result since they sample from generally smooth objective functions in a low signal-to-noise regime. However, in cases where a directional estimate per wavenumber or beam group is needed, the MCMC iteration length can be adjusted.

3.1.2 Constraining direction estimates with other data products

Sampling of the objective function eq. (11) as described in sec. 3.1 results in a joint distribution of most likely incident angles and phases. These joint distributions may have multiple equally likely incident angles (Fig. 6d blue area) due to the limited across-track observations and distortion. To break the symmetry in the marginalized PDF of incident angles (Fig. 6e) we define a prior $P_\theta(\theta, k)$ in the objective function using ridge-regression (Appendix B). The effect of the prior on the joint- and marginalized distribution is shown by comparing Figure 6 b and c with d and e. Here we inform the prior with WW3 global hindcast wave-partitions (Tolman, 2009, using the Integrated Ocean Waves for Geophysical and other Applications (IOWAGA) hindcast)). WW3 must be treated with caution due wind-observational biases in the Southern Ocean (Belmonte Rivas and Stoffelen, 2019; Hell et al., 2020). This wave hindcast is currently the only readily available dataset for this global purpose, and priors from observational datasets would improve the quality of this data and the overall wave inversion.

The level of certainty in the WW3 prior is expressed in the hyper parameter β_θ and the performance of the MCMC sampling is sensitive to its value (eq. 11). Since a validation of the WW3 prior is limited, we set $\beta_\theta = 2$. Its effect on the objective function can be seen by comparing the shading in figure 6 b and d. The choice of $\beta_\theta = 2$ leads to the desired result in breaking the directional ambiguity while not fully determining the incident angle distribution (Fig. 7a). Other values of β_θ are tested, but higher values tend to over fit to the prior, and lower values do not break the ambiguity.

This method is limited to angles of about $\pm 85°$. Oblique incidence angle can not be captured by this methods. In addition, the model has a $180°$ ambiguity such that samples in the $+95°$ to $-95°$ arc, that are waves coming from higher latitudes rather than from the equator, would be equally possible. However given the geography of the Antarctic coast for tracks considered here, these are less plausible.

3.2 Two-dimensional spectra in along-track data

With the spectral (sec. 2.2) and angle (sec. 3.1) estimates, we now can describe waves observed along-track in terms of their two-dimensional wavenumber spectra (Fig. 8). The estimated wavenumber amplitudes $\hat{\mathbf{b}}$ (eq. 2) are corrected by $\cos^{-1}(\theta)$ using the most likely incident angle (sec. 3.1, Fig. 7b) resulting in the corrected wavenumber spectrogram (Fig. 8a). We use

https://doi.org/10.5194/egusphere-2022-842
Preprint. Discussion started: 12 September 2022

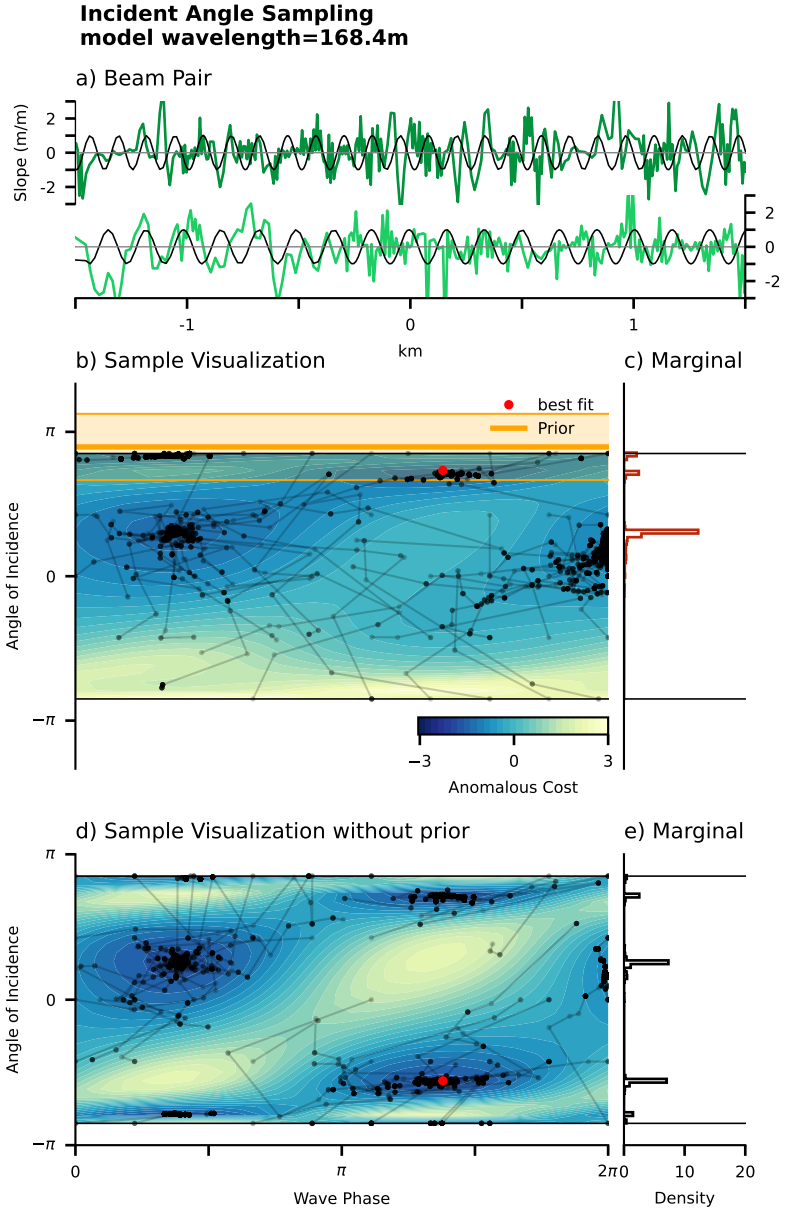

Figure 6. MCMC angle estimate using a monochromatic wave model with and without a prior P_θ. (a) Data of the beam pair gt1l and gt1r (light and dark green) and model (black, eq. 10) for a segment of Track 3 (granule `05160312`, centered at $X_i = 62.5$ km. (b). The objective function with prior P_θ is sampled using a brute-force method (shading) and MCMC (black dots and lines). The prior angle θ_0 and prior uncertainty σ_θ for this wavelength (168.4 meter) are shown as thick orange line and shading. The best fit using a dual-annealing method is shown is shown as red dot (Tsallis and Stariolo, 1996). (c) Marginal PDF of the incident angle θ from MCMC sampling. (d) and (e) same as (b) and (c) but without the prior P_θ.

https://doi.org/10.5194/egusphere-2022-842
Preprint. Discussion started: 12 September 2022

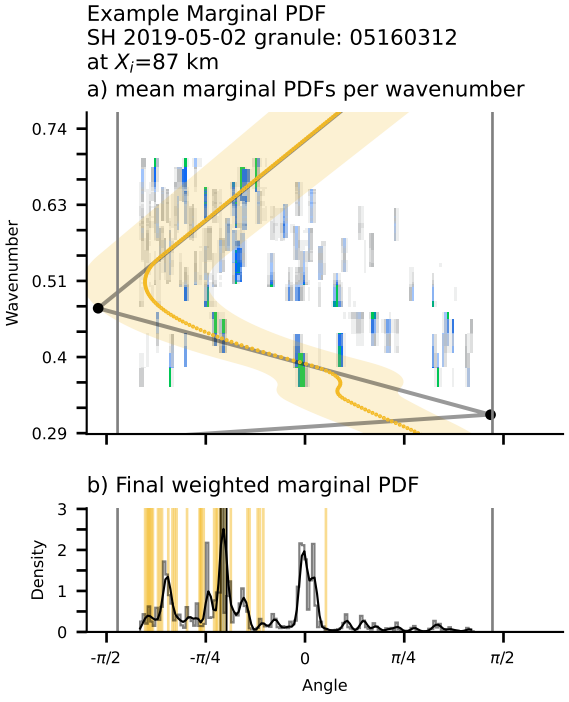

Figure 7. Influence of the WW3 prior on the marginal PDFs of Track 3 (granule `05160312`) at $X_i = 87$ km. (a) Mean marginal PDFs for all beam-pairs as a function of wavenumber. The WW3 spectral partitions are shown as black dots and the interpolated prior $\theta_{0,i}$ and its spread $\sigma_{\theta,i}$ (eq. B1) are shown as orange line and orange shading. (b) The smoothed weighted mean across the pairs of the most likely incident angle is shown as black thick line and the WW3 priors for all wave numbers used as orange lines.

the most likely angle along the track, although the above analysis can provide angle distributions for each segment X_i and wavenumber k (sec. 3.1.2, Fig. 8b).

The corrected power spectrum and directional distribution (Fig. 8 a,b) can be expressed as directional surface wave spectra every 12.5 km in the MIZ, similar to conventional surface wave buoys (Fig. 8 c to e). This permits tracking the attenuation of wave energy per frequency in MIZ. In the case of Track 3 (granule `05160312`) for example, we see a migration of the peak wavelength from about 275 meters to about 300 meters within 12.5 km (Fig. 8 d,e) as shorter waves tend to attenuate faster. Future work will systematically use this analysis to understand attenuation in the MIZ.

4 Decomposition of along-track data to waves and surface roughness

The estimate of the wave signal from sec. 2.3 can be used to decompose wave and ice surface variability. Each photon retrieval is a super-position of ocean waves and sea ice variability like surface roughness, floe-size, and free board height. A decomposition of surface variability between waves and ice can rely on the coherence of across-beam wave statistics, as well as their common

https://doi.org/10.5194/egusphere-2022-842
Preprint. Discussion started: 12 September 2022

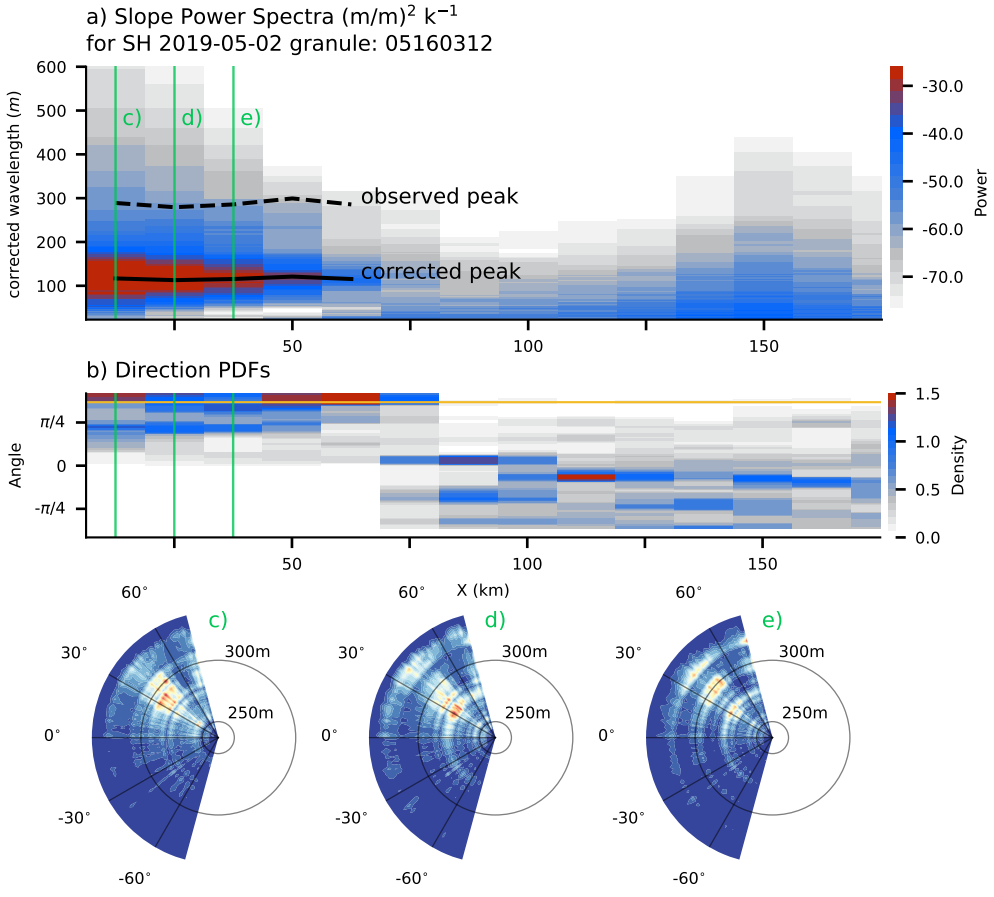

Figure 8. Final estimate of the power (a), directional (b), and joint (c,d,e) surface slope spectra every 12.5 km along an ICESat-2 beam (example Track 3). (a) The angle-corrected spectrogram as a function of estimated wavelength λ and distance from the ice-edge X. The power spectral wavelength where corrected by about a factor of three due to a peak incident angle of about 66° (orange line in b). The observed and corrected peak wavelengths λ' and λ are shown as dashed and solid black line. (b) Mean directional PDF between $\pm 85°$ every 12.5 km. (c) to (e) Rolling-mean smoothed directional wave spectra at the positions indicated at the respective green lines in (a) and (b).

noise level in wavenumber space. For the purpose of decomposing the data we define similar signal-to-noise levels across beams in each 25 km segment (Fig. 5 a to f).

The results of section 2.3 are used to delineate ATL03 photon heights between wave and sea ice surface variability. We construct a binned wave height field along-track from the GFT-derived surface slope spectrum, by filtering out high-wavenumber components that likely do not correspond to swell waves. This low-pass filter is defined by a cutoff-wavenumber k_c, which is the first wavenumber where the power spectrum changes slope. A change in the power-spectral slope in log-log scaling from the expected slope of surface wave spectra ($k^{-5/2}$ or similar, Toba, 1973) to horizontal indicated a change in the signal-to-noise regime in the data (Fig. 9). Hence, horizontal slopes at high wavenumber indicates Gaussian (white) noise, while steep wavenumber-slope are the result of wave-wave interaction (Kitaigorodskii, 1962; Hasselmann et al., 1973). The critical

https://doi.org/10.5194/egusphere-2022-842
Preprint. Discussion started: 12 September 2022

wavenumber k_c between both regimes is found using piecewise regression on the weighted cross-beam log-log power spectrum (Fig. 9, Pilgrim, 2021).

For illustrative purposes we define a low-pass filter by setting k_c as the cut-off wavenumber. This low-pass filter potentially creates artificial ringing in real space and for better results this should be replaced by a more complex filter design. Here, wavenumbers higher than k_c are excluded from the wave height model of all beams (Fig. 10a gray and blue lines and gray area in inlet) by truncating the wavenumber space of the slope model $\mathbf{p}$. From this truncated slope model we can directly construct a coefficient matrix for the wave-height model $\hat{\mathbf{z}}$ for each individual beam by integrating in wavenumber space. The coefficient matrix of the wave-height model $\hat{\mathbf{z}}$ is

$$\hat{\mathbf{d}} = [-b_1, -b_2, ..., -b_c, a_1, ...a_c,]^T,$$

where b_c and a_c are the model amplitudes corresponding the the cutoff frequency k_c (note the integration of the trig-formula changes order and sign of the indices). The reconstructed wave-height model $\hat{\mathbf{z}}$ can then be directly calculated from the original regressor matrix,

$$\hat{\mathbf{z}} = \mathbf{H}\,\hat{\mathbf{d}}\,{\mathbf{k_c}}^{-1}, \tag{12}$$

with $\mathbf{k_c} = [k_1, k_2, ..., k_c, k_1, ..., k_c]^T$ as shown in figure 10b blue line. The residual between the height model $\hat{\mathbf{z}}$ and the observed smoothed photon heights $\mathbf{z}$, $\mathbf{z}_{free} = \mathbf{z} - \hat{\mathbf{z}}$, is an estimate of the freeboard height absent the influence of waves (Fig. 10d). The residual $\mathbf{z}_{free}$ has similar data density to the original ATL03 photon retrievals but may reveal secondary, non-wavelike structures in the photon heights as shown in figure 10d. We provide additional examples in suppl. Fig. S6 and S7.

Decomposing heights into wave and sea ice components allows us to estimate the fraction of the total height variance that is neither due to waves nor photon variance on scales shorter than the 10-meter stencil. As shown in figure 10e, the majority of the total variance is due to the photon variance around its 20-meter stencil mean for scales smaller then the stencil (Fig. 10d red line and black dots, Kwok et al., 2021). In this particular track wave variance than comprises between another 20% to 50% of total photon height variance. The remaining variance about, about 5% to 20%, due to neither waves nor the photon cloud, is from differences in the observed and modeled wave heights, $\hat{\mathbf{z}}$ and $\mathbf{z}$. We assume this is to sea-ice-related variability. The distribution of the residual statistics is, by model design, approximately Gaussian (Fig. 3e) and hence non-wave signals with non-linear imprint could contaminate the wave estimate and decomposition. In general, this decomposition removes waves as the dominant source of variance on scales larger than 20 meters, allowing for additional analysis of the residual signal, and more consistent surface height signals in wave-affected and low-sea ice regions.

5 Discussion

ICESat-2 photon data frequently shows wave-like signals in sea ice and these substantially impacts the marginal ice zone. In this paper, we show, for the first time, how paired laser-altimeter observations can be converted into directional surface wave spectra. We describe a two-part algorithm that efficiently decomposes the IS2 photon retrievals into a surface wave signal

https://doi.org/10.5194/egusphere-2022-842
Preprint. Discussion started: 12 September 2022

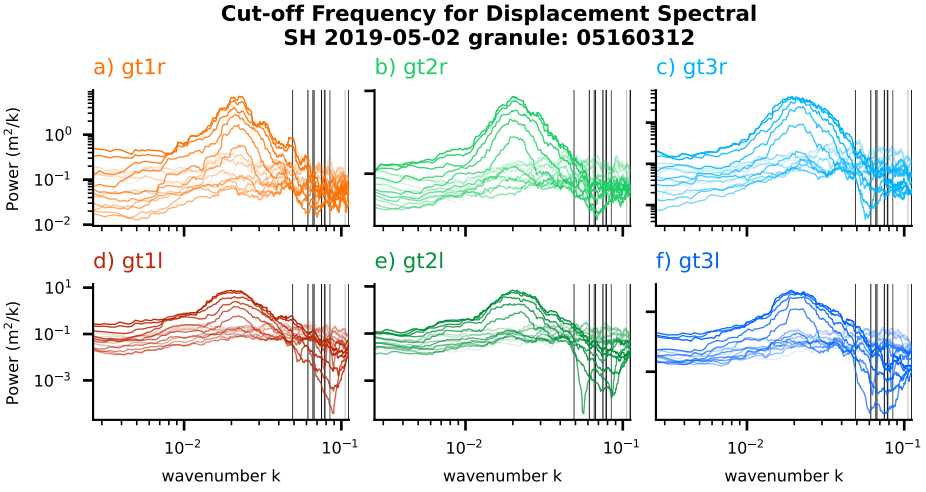

Figure 9. Sections of derived displacement power spectra $\hat{\tilde{S}}_h$ for Track 3 (Fig. 8) for each beam (a to f). The black lines show the position of the estimated cut-off wavenumber k_c based on piece-wise regression on the weighted mean of all beams. Darker colored lines show sections closer to the sea ice edge and lighter colors show sections further into the sea ice.

as well as variability due to sea ice. The 1st part of the algorithm is based on a linear inversion method to fit wavenumber coefficients to the ATL03 data (sec. 2.2 to 2.4), and the 2nd part uses a non-linear inversion method that optimizes for most-likely wave incident angles (sec. 3.1).

The combined method than provides a highly-resolved 2D-surface wave spectra every 12.5 km along each IS-2 track (Fig. 8a,b) as well as an improved surface height estimate when the wave signal is removed (Fig. 10). The surface wave estimate relies on the one hand on the redundancy across beams to optimize the signal-to-noise ratio in wavenumber space and on the other hand on the difference across beams for the angle inversion. The iterative solution proposed here leads to an interpretation of the IS-2 track as streak of two-dimensional wave spectra, including error estimates on each variable (Fig. 8c to e).

We identify the range of wavenumbers that contain wave energy in each segment by establishing a dynamic noise level (sec. 4). Removing the wave energy as a dominant source of variance reveals additional structure in the ATL03 photon cloud data that is not as readily present in the ATL07, or other higher level products (Fig. 10d, or suppl. Fig. S6 and S7), either because it is obscured by wave signals or the data is not present. A removal of the wave signal may have substantial benefits for classifying photon data for ATL07 products and above. Not removing the wave signal likely leads to aliasing effect of the waves into the freeboard height (compare panel b and d in figure 10).

Our quantification of wave energy allows for an improved understanding of photon variance. While in three example tracks have a substantial amount of variance in photon height on scales smaller then 20-meters (Fig. 11a,c,e gray area), the variance on scales longer than 20-meters is clearly dominated by the effect of waves (Fig. 11a,c,e blue area). Especially in the MIZ,

https://doi.org/10.5194/egusphere-2022-842
Preprint. Discussion started: 12 September 2022

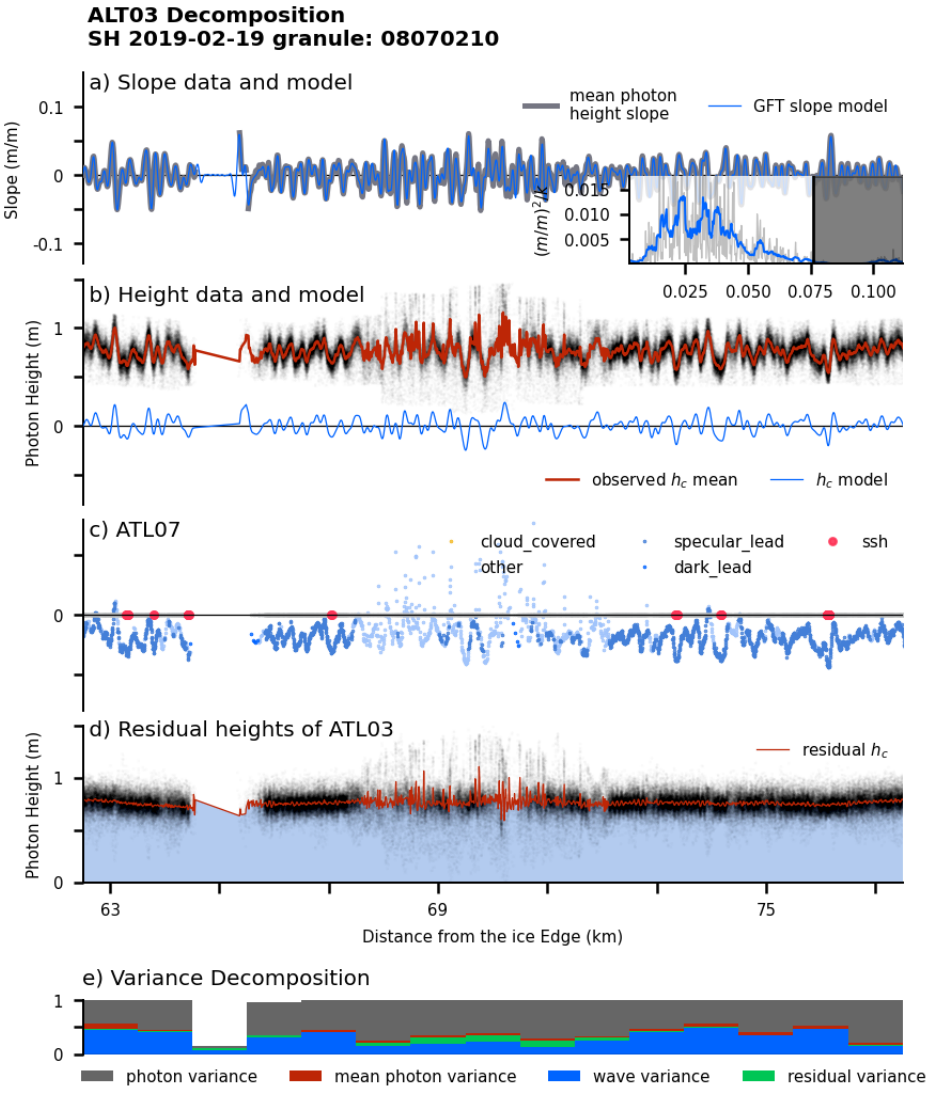

Figure 10. Variance decomposition of the photon-cloud data (ATL03) based on the GFT of example Track 2. (a) The observed mean surface height slope $\mathbf{b}$ is shown in gray and the truncated model $\hat{b}$ in blue. The inset shows the corresponding smoothed spectral amplitudes and cut-off wavenumber k_c as a black line. (b) The observed photon cloud is shown as black dots, re-binned data $\mathbf{z}$ as a red line (sec. 2.1), and the reconstructed surface heights as a thin blue line $\hat{\mathbf{z}}$ (eq. 12). (c) Corresponding ATL07 surface heights product shown as in figure 2. (d) Residual photon heights (black) and binned heights (red) using $\hat{\mathbf{z}} - \mathbf{z}$. (e) Variance fraction every kilometer with the fraction due to the photon cloud (gray), the truncated wave model $\hat{\mathbf{z}}$ (blue), variance of wavenumber $> k_c$ (green), and the residual of the model $\mathbf{r}$ (red, eq. 1).

only a small fraction of this re-binned variance is due to non-wavy features of the surface (Fig. 11a and e gray-blue area at 0 - 50 km from the ice edge).

This wave-induced variance in photon cloud of ATL03 can, under certain conditions, also be captured by ATL07. However, we suggest that the ATL07 algorithm also can potentially capture an aliased wave signal, or can fail to provide a sufficient sea-

https://doi.org/10.5194/egusphere-2022-842
Preprint. Discussion started: 12 September 2022

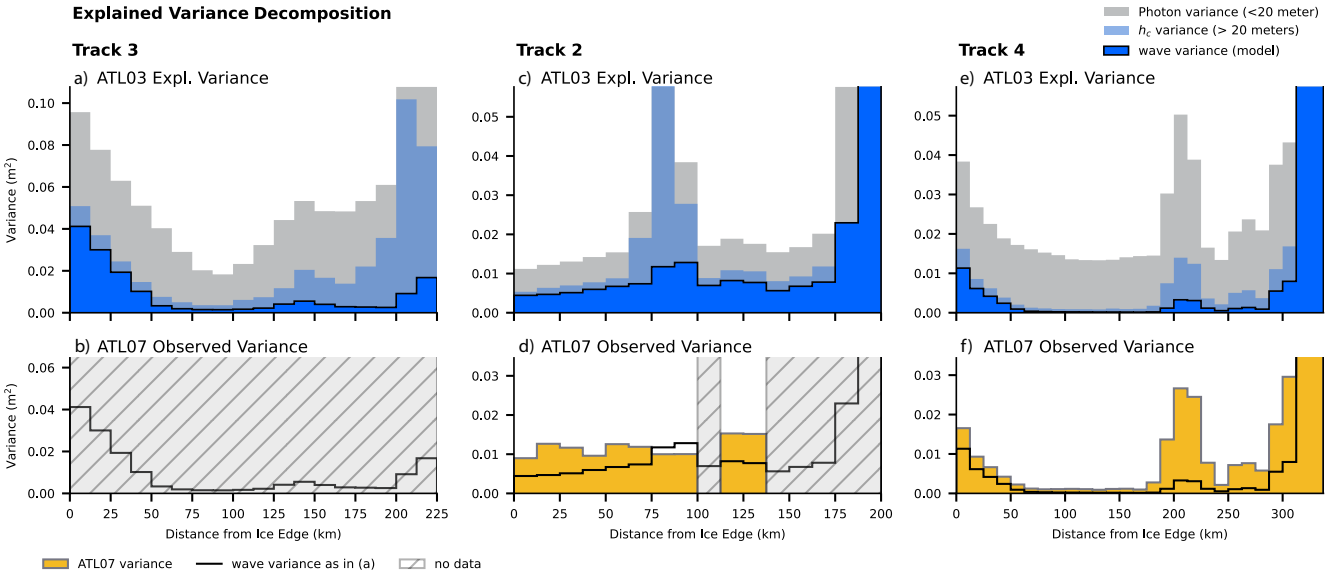

Figure 11. Variance decomposition of ATL03 photon cloud data and comparison with ATL07 data. (a) Across-beam averaged variances for Track 3 (granule `05160312`, see suppl. Table). The photon cloud variance is shown in black (same as Fig. 10b black dots), the variance of the 20-meter stencils is shown in light blue (same as Fig. 10b red line), and the variance of the low-pass filtered wave model in dark blue with a black outline (same as Fig. 10b blue line). (b) Variance of ATL07 based on the provided segment heights. Gray hatched areas indicate no data in ATL07 as for this track. Black line is repeated from panel (a) for comparison. (c and d) Same as (a) and (b) but for Track 2 (granule `08070210`). (e and f) Same as (a) and (b) but for Track 4 (granule `05180312`)

ice height product at all. While in the case of Track 3 (Fig. 11a,b), waves clearly affect the observation, ATL07 does not provide data in this region (see also suppl. Fig. S2) and so our inversion method using ATL03 allows for improved MIZ freeboard data. In other cases, like Track 2 (Fig. 11d), ATL07 does provide data at some but not all locations along-track, even though there is a high photon density throughout the track.

In the MIZ, ATL07 variance can exceed the variance estimates of waves, indicating a potential aliasing of wave-induced signal to other scales (Fig. 11d). This aliasing can be due to the binning of data based on photon counts which result in varying bin length. Varying bins-length potentially sub-samples the wave's energy at scales on, or around the Nyquist frequency of the dominant waves. Since both the wavelength and photon density highly vary, it is generally unknown whether or not the photo-count based measure samples these wavelengths correct and does not negatively affect freeboard retrievals or wave energy estimates in the MIZ .

The provided algorithm has particular use when applied at scale. We expect $10-15\%$ of the IS-2 tracks in polar regions to be dominated by waves (Brouwer et al., 2021). That implies roughly $3-4.5\times10^3$ cases of diverse wave observation in the MIZ (as of June 2022) to sample the large space of wave-ice interaction, which is likely enough to better constrain sea-ice wave interactions. Because IS-2 can also record freeboard heights, floe sizes, and sea ice types, this analysis can provide complimentary sea ice information to better constrain dynamics in the MIZ. In particular this analysis will be used to

https://doi.org/10.5194/egusphere-2022-842
Preprint. Discussion started: 12 September 2022

a) provide data for case studies of wave-ice interaction in the MIZ,

b) statistically constrain wave attenuation in sea ice (Fig. 5), and

c) leverage the wave-removed residual signal to improve ice classification (Fig. 10 d).

We chose a generalized Fourier transform (GFT) method instead of more common methods like DFT, or Lomb-Scargle (LS, sec. 2.2, Lomb, 1976; Scargle, 1982; Wunsch, 1996; Kachelein et al., 2022). In contrast to the DFT and LS, the GFT is variance conserving method that can be applied to unstructured data and does not require periodicity over an (arbitrary) window length.

The GFT is customize-able to the wavenumbers of interest and additionally provides uncertainty bounds on all parameters. In turn, it comes with the requirement to apriori know what spectral resolution is needed. Given Atlas's high resolution photon cloud data, we chose to resolve the plausible wavenumber range for surface waves on a resolution about twice the one of the DFT. Other, more targeted, narrow-banded wavenumber-spaces are possible, but here we choose wavenumber ranges that are the most general for surface waves. A higher resolutions especially at long wavenumber allows us to provide new insights in how narrow-banded the surface wave field is; a parameter that is related to the surface's curvature and likely important for wave-induced sea-ice breakup (Meylan and Squire, 1994).

A major advantage of the GFT is that it can be extended to inversions of the wave field for each IS2 track by coupling neighboring or overlapping segments, similar to Kalman inversion methods. We illustrate this by simply iterative updating the data segments and models priors (sec. 2.4, Fig. 4). This coupling of inversions along segments advances the task on hand to solving the coupled inversions consistently along each beam, rather then independently for each segment. The same idea can be extended by coupling the model prior $\mathbf{P}$ across beams. This coupled approach ensures smoothly varying wave statistics along and across-track, with the amount of smoothness tuned through the amplitude of $\mathbf{P}$ in (eq. 6).

The inversion for the wave's incident angle is based on the cross-beam coherence (sec. 3). The coherence between two beams is limited by the geometry (Fig. 1b), a difficult-to-estimate properties of the wave field (i.e. its "groupiness", suppl. Fig. S7), as well as observational noise (sec. 3.1). We choose to approach this low signal-to-noise problem with a super-sample of marginal distributions derived from independent MCMC samples of monocromatic plane waves. The unweighted mean of this method across all wavenumbers is similar to the lag-cross correlation of the beam pair. However, by focusing on a limited set of energy-containing wavenumbers, the signal-to-noise-ratio improves above a lagged cross-correlation approach. Limiting the sample to the most energetic waves and using a prior is what enables an inversion of the approximate wave angle (Fig. 7d). Alternatively, ensemble-based approaches could search for a common direction across wavenumbers simultaneously, but the presented MCMC method has an advantage in that it can sample multiple minima in the objective function. Multiple minima, and therefore multiple potential incidence angles, are a plausible result for two-dimensional wave fields when observed only along segments (Fig. 6).

The low signal-to-noise of the angle inversion requires regularization (sec. 3.1). Since directional wave observation co-located with IS2 tracks are sparse and not readily available, we relied on Wave Watch III (WW3) hindcast models as a prior (IOWAGA Tolman, 2009). The wave hindcasts may perform sufficiently well in the Northern Hemisphere but are known to have limitations in the Southern Ocean MIZ, potentially due to wind biases (Belmonte Rivas and Stoffelen, 2019; Hell et al.,

https://doi.org/10.5194/egusphere-2022-842
Preprint. Discussion started: 12 September 2022

2020, 2021b). The lack of certainty in WW3's peak direction and frequency is expressed the value of the hyper parameter β_θ (eq. 11). A value of $\beta_\theta = 2$ leads to the desired behavior of breaking the symmetry (compare shading in figure 6 b and d) but not imposing the optimization result through the prior (Fig. 7d blue and orange lines).

The angle inversion is limited to the geometry of the observation and the nature of the surface wave statistics (sec. 3.1). Waves coming from steep angels compared to the IS-2 track cannot be resolved, which limits successful 2D-wave field estimates to cases where we have an educated guess of an incident angle that is not too steep. This problem may be overcome by using better, observationally-based priors, or enriching our WW3 priors with data from other sources.

While the here developed methods are customized for ICESat-2 photon retrievals, this approach is applicable to any unstructured quasi-instantaneous observation of a two-dimensional wave field. In the case of IS-2, cross-track information is limited, but other future remote-sensing methods may have complimentary information about the surface wave field. Such an inversion could combine data from IS-2, SAR, and CFOSat to help constrain the surface wave filed in the MIZ or the open ocean (Collard et al., 2022).

Code and data availability. The algorithms are available through Hell (2022a, DOI: 10.5281/zenodo.6908645) and data are available through Hell (2022b, DOI: 10.5281/zenodo.6928350). The IS-2 ATL03 data (Neumann et al., 2021) and ATL07/10 data (Kwok et al., 2021) is available through NSIDC (https://nsidc.org/data/icesat-2/data-sets), or OpenAltimetry (https://openaltimetry.org/data/icesat2/, Khalsa et al., 2020). The wave model data are available through the Integrated Ocean Waves for Geophysical and other Applications (IOWAGA) project: ftp.ifremer.fr/ifremer/cersat/products/gridded/wavewatch3/hindcast/. The analysis uses and modifies the *icesat2 toolkit* (https://read-icesat-2.readthedocs.io/)

Appendix A: GFT priors

A1 Data Prior $\mathbf{R}$

We define the data prior $\mathbf{R}$ based on the surface slope uncertainty, as

$$\mathbf{R} = \beta_R \, \sigma(\mathbf{b})^2 \, \frac{\boldsymbol{\sigma}_h}{\Delta x}$$

where the stencil width is $\Delta x = 20$ meters, $\sigma(\mathbf{b})$ is the standard deviation of the data $\mathbf{b}$ within the segment, $\boldsymbol{\sigma}_h$ is the vector of standard deviation of each data point (each stencil, sec. 2.1), and β_R is a tuning parameter that determines the ratio of the model and data priors in eq. 6 (Fig. 2 blue lines). The standard deviation, or error, of the data is divided by the stencil size to get an error in units of surface slope and $\mathbf{R}$ is amplified by the variance of the data to scale it against the model prior.

To avoid over-fitting the ratio of the model prior $\mathbf{P}$ and data prior $\mathbf{R}$ has to be adjusted. For this we try different values of β_R and set it to 10^2 such that the distribution of the residual $\mathbf{r}$ is approximately Gaussian and that

$$||\mathbf{r}|| = ||\mathbf{b} - \mathbf{H}\,\hat{\mathbf{p}}|| \approx 1,$$

https://doi.org/10.5194/egusphere-2022-842
Preprint. Discussion started: 12 September 2022

as shown in Figure 3e. At locations with no data this results in a model decay to zero (Fig. 3 orange lines) on scales similar to the data's auto correlation.

A2 Model Prior P

As described in section 2.4, the GFT's prior is initially derived from a PM-spectrum that is fitted to a DFT of the segment data (Fig. A1a gray and black line). The initial prior $\mathbf{P}_{init}$ is then defined as the peak-normalized PM-spectrum multiplied by the data variance $\sigma(\mathbf{b})^2$ plus a 10% noise floor (Fig. A1a green line). The power of the resulting GFT model coefficients $\hat{\mathbf{p}}$ is then shown as red line in figure A1a. For a segment i with a successfully inversion in the previous segment $i-1$ we use a smoothed power spectrum based on $\hat{\mathbf{p}}_{i-1}$ to derive $\mathbf{P}_i$ (fig. A1b green line, sec. 2.4).

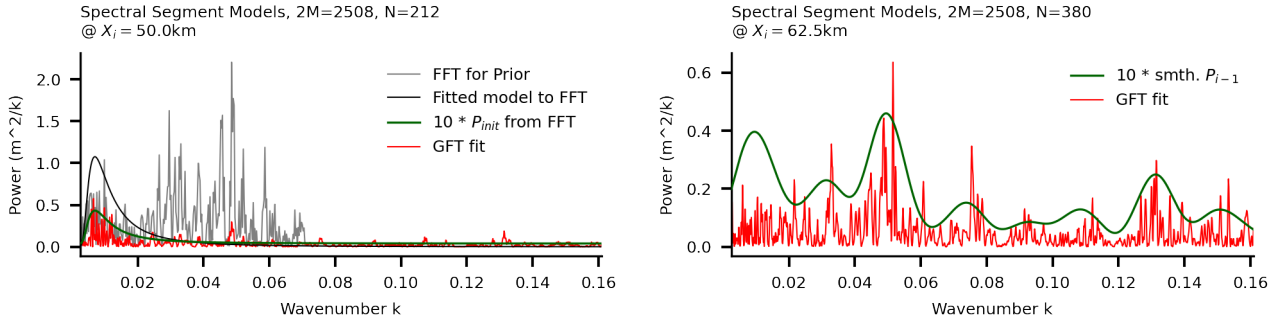

Figure A1. Two GFT fit examples at $X_i = 50$ km (left) and $X_i = 62.5$ km (right) with the DFT of the data in gray, the fitted PM-model in black, the rescaled PM-model as prior P_{init} (multiplied by a factor of 10), and the final GFT inversion expressed as power spectra in red. The number of $2M$ model parameters and number of N data points are given in the title.

Appendix B: Wave-watch III Prior

The prior in eq. 11 uses an incident angle $\theta_0(k)$ with an uncertainty $\sigma_\theta(k)$, defining the prior

$$P_\theta(\theta, k) = \left(\frac{\theta_0(k) - \theta}{\sigma_\theta(k)} \right)^2 . \tag{B1}$$

Both variables in the prior have to be taken from other data sources than IS-2 and here they are derived from WW3 global hindcast wave-partitions (Tolman, 2009, using the Integrated Ocean Waves for Geophysical and other Applications (IOWAGA) hindcast)) and depend on wavenumber. The WW3 hindcast data is selected in a box around the most equatorward photons in ICESat-2 (suppl. Fig. S4 and. sec. 2.1). In cases where this box is within the sea-ice mask of WW3 it is moved equatorward along the IS-2 track until at least $2/3$ of the box's grid cells are not covered by the WW3 sea-ice mask.

Within each box, the mean of the peak period, peak direction, and directional spread is calculated for each of the five WW3 wavenumber partitions (Fig. 7a black dots). These partitions are interpolated and smoothed to the k_i wave numbers of interest

https://doi.org/10.5194/egusphere-2022-842
Preprint. Discussion started: 12 September 2022

to provide a best guess of the wavenumber-dependent peak direction and spread (Fig. 7a orange line and shading). Note that it is hard to validate the WW3 partitions in the Southern Ocean due to a lack of contemporaneous in-situ observations. The a lack of certainty in the wave-hindcast in combination with (any) smoothing procedure can lead to biases in the directional prior. Hence, we do not expect direct alignment of the WW3 wave directions and those observed in ICESat-2 observations. The WW3 incident angle is here solely used to reduce ambiguities in the objective function (Fig. 6 b and d and Figure 7) and can give a *preferred* incident wave angle, rather than a certain estimate of the dominant wave angle (Fig. 7).

Author contributions.

MH developed and programmed the proposed algorithm. MH and CH collaboratively wrote the paper.

Competing interests.

We have no no competing interests.

Acknowledgements. We thank Bruce Cornuelle and Baylor-Fox Kemper for discussing depths and caveats of the proposed algorithms. C.H. and M.H. were supported by Schmidt Futures—a philanthropic initiative that seeks to improve societal outcomes through the development of emerging science and technologies.

https://doi.org/10.5194/egusphere-2022-842
Preprint. Discussion started: 12 September 2022

References

Ardhuin, F., Stopa, J., Chapron, B., Collard, F., Smith, M., Thomson, J., Doble, M., Blomquist, B., Persson, O., Collins, C. O., and Wadhams, P.: Measuring ocean waves in sea ice using SAR imagery: A quasi-deterministic approach evaluated with Sentinel-1 and in situ data, Remote Sensing of Environment, 189, 211–222, https://doi.org/10.1016/j.rse.2016.11.024, 2017.

Belmonte Rivas, M. and Stoffelen, A.: Characterizing ERA-Interim and ERA5 Surface Wind Biases Using ASCAT, Ocean Sci., 15, 831–852, https://doi.org/10.5194/os-15-831-2019, 2019.

Brouwer, J., Fraser, A. D., Murphy, D. J., Wongpan, P., Alberello, A., Kohout, A., Horvat, C., Wotherspoon, S., Massom, R. A., Cartwright, J., and Williams, G. D.: Altimetric observation of wave attenuation through the Antarctic marginal ice zone using ICESat-2, The Cryosphere, 367, https://doi.org/10.5194/tc-2021-367, 2021.

Collard, F., Marié, L., Nouguier, F., Kleinherenbrink, M., Ehlers, F., and Ardhuin, F.: Wind-Wave Attenuation in Arctic Sea Ice: A Discussion of Remote Sensing Capabilities, J. Geophys. Res. Oceans, 127, e2022JC018 654, https://doi.org/10.1029/2022JC018654, 2022.

Foreman-Mackey, D., Hogg, D. W., Lang, D., and Goodman, J.: Emcee: The MCMC Hammer, Publ. Astron. Soc. Pac., 125, 306–312, https://doi.org/10.1086/670067, 2013.

Hasselmann, K., Barnett, T. P., Bouws, E., Carlson, H., Cartwright, D. E., Enke, K., Ewing, J. A., Gienapp, H., Hasselmann, D. E., Kruseman, P., Meerburg, A., Müller, P., Olbers, D. J., Richter, K., Sell, W., and Walden, H.: Measurements of Wind-Wave Growth and Swell Decay during the Joint North Sea Wave Project (JONSWAP), Ergänzungsheft 8-12, 1973.

Hell, M.: Code for Directional Surface Wave Spectra And Sea Ice Structure from ICEsat-2 Altimetry without Data, Zenodo, https://doi.org/10.5281/zenodo.6908645, 2022a.

Hell, M.: Data for Directional Surface Wave Spectra And Sea Ice Structure from ICEsat-2 Altimetry, https://doi.org/10.5281/zenodo.6928350, 2022b.

Hell, M. C., Cornuelle, B. D., Gille, S. T., Miller, A. J., and Bromirski, P. D.: Identifying Ocean Swell Generation Events from Ross Ice Shelf Seismic Data, J. Atmos. Oceanic Technol., 36, 2171–2189, https://doi.org/10.1175/JTECH-D-19-0093.1, 2019.

Hell, M. C., Gille, S. T., Cornuelle, B. D., Miller, A. J., Bromirski, P. D., and Crawford, A. D.: Estimating Southern Ocean Storm Positions With Seismic Observations, J. Geophys. Res. Oceans, 125, e2019JC015 898, https://doi.org/10.1029/2019JC015898, 2020.

Hell, M. C., Ayet, A., and Chapron, B.: Swell Generation Under Extra-Tropical Storms, J. Geophys. Res. Oceans, 126, e2021JC017 637, https://doi.org/10.1029/2021JC017637, 2021a.

Hell, M. C., Cornuelle, B. D., Gille, S. T., and Lutsko, N. J.: Time-Varying Empirical Probability Densities of Southern Ocean Surface Winds: Linking the Leading Mode to SAM and Quantifying Wind Product Differences, J. Clim., 34, 5497–5522, https://doi.org/10.1175/JCLI-D-20-0629.1, 2021b.

Horvat, C.: Floes, the Marginal Ice Zone, and Coupled Wave-Sea-Ice Feedbacks, Phil Trans Roy Soc. A., https://doi.org/10.1098/rsta.2021.0252, 2022.

Horvat, C., Tziperman, E., and Campin, J.-M.: Interaction of sea ice floe size, ocean eddies, and sea ice melting, Geophysical Research Letters, 43, 8083–8090, https://doi.org/10.1002/2016GL069742, 2016.

Horvat, C., Blanchard-Wrigglesworth, E., and Petty, A.: Observing waves in sea ice with ICESat-2, Geophysical Research Letters, https://doi.org/10.1029/2020GL087629, 2020.

Kachelein, L., Cornuelle, B. D., Gille, S. T., and Mazloff, M. R.: Harmonic Analysis of Non-Phase-Locked Tides with Red Noise Using the Red_tide Package, J. Atmospheric Ocean. Technol., -1, https://doi.org/10.1175/JTECH-D-21-0034.1, 2022.

https://doi.org/10.5194/egusphere-2022-842
Preprint. Discussion started: 12 September 2022

Khalsa, S. J. S., Borsa, A., Nandigam, V., Phan, M., Lin, K., Crosby, C., Fricker, H., Baru, C., and Lopez, L.: OpenAltimetry - Rapid Analysis and Visualization of Spaceborne Altimeter Data, Earth Sci Inform, https://doi.org/10.1007/s12145-020-00520-2, 2020.

Kitaigorodskii, S. A.: Applications of the Theory of Similarity to the Analysis of Wind-Generated Wave Motion as a Stochastic Process, Izv Geophys Ser Acad Sci USSR, 1, 105–117, 1962.

Kwok, R., Petty, A., Cunningham, G., Markus, T., Hancock, D., Morison, J. H., Palm, S. P., Farrell, S. L., Ivanoff, A., Wimert, J., and ICESat-2 Science Team: ATLAS/ICESat-2 L3A Sea Ice Height, Version 3 [ATL07/10, 2022-04-04], https://doi.org/10.5067/ATLAS/ATL07.003, 2021.

Lomb, N. R.: Least-Squares Frequency Analysis of Unequally Spaced Data, Astrophys Space Sci, 39, 447–462, https://doi.org/10.1007/BF00648343, 1976.

Longuet-Higgins, M. S.: Statistical Properties of Wave Groups in a Random Sea State, Philos. Trans. R. Soc. Lond. Ser. Math. Phys. Sci., 312, 219–250, https://doi.org/10.1098/rsta.1984.0061, 1984.

Longuet-Higgins, M. S. and Deacon, G. E. R.: The Statistical Analysis of a Random, Moving Surface, Philos. Trans. R. Soc. Lond. Ser. Math. Phys. Sci., 249, 321–387, https://doi.org/10.1098/rsta.1957.0002, 1957.

Lygre, A. and Krogstad, H. E.: Maximum Entropy Estimation of the Directional Distribution in Ocean Wave Spectra, J. Phys. Oceanogr., 16, 2052–2060, https://doi.org/10.1175/1520-0485(1986)016<2052:MEEOTD>2.0.CO;2, 1986.

Marechal, G. and Ardhuin, F.: Surface Currents and Significant Wave Height Gradients: Matching Numerical Models and High-Resolution Altimeter Wave Heights in the Agulhas Current Region, J. Geophys. Res. Oceans, 126, e2020JC016 564, https://doi.org/10.1029/2020JC016564, 2021.

Menke, W.: Geophysical Data Analysis: Discrete Inverse Theory, Academic press, 2018.

Meylan, M. and Squire, V. A.: The Response of Ice Floes to Ocean Waves, J. Geophys. Res. Oceans, 99, 891–900, https://doi.org/10.1029/93JC02695, 1994.

Neumann, T. A., Brenner, D., Hancock, D., Robbins, J., Saba, K., Harbeck, K., Gibbons, A., Lee, J., Luthcke, S. B., and Rebold, T.: ATLAS/ICESat-2 L2A Global Geolocated Photon Data, Version 5. [ATL03, 2022-04-04], https://doi.org/10.5067/ATLAS/ATL03.005, 2021.

Pierson, W. J. and Moskowitz, L.: A Proposed Spectral Form for Fully Developed Wind Seas Based on the Similarity Theory of S. A. Kitaigorodskii, J. Geophys. Res., 69, 5181–5190, https://doi.org/10.1029/JZ069i024p05181, 1964.

Pilgrim, C.: Piecewise-Regression (Aka Segmented Regression) in Python, J. Open Source Softw., 6, 3859, https://doi.org/10.21105/joss.03859, 2021.

Rapley, C. G.: First Observations of the Interaction of Ocean Swell with Sea Ice Using Satellite Radar Altimeter Data, Nature, 307, 150–152, https://doi.org/10.1038/307150a0, 1984.

Scargle, J. D.: Studies in Astronomical Time Series Analysis. II. Statistical Aspects of Spectral Analysis of Unevenly Spaced Data., Astrophys. J., 263, 835–853, https://doi.org/10.1086/160554, 1982.

Squire, V. A.: Of ocean waves and sea-ice revisited, Cold Regions Science and Technology, 49, 110–133, https://doi.org/10.1016/j.coldregions.2007.04.007, 2007.

Squire, V. A.: A Fresh Look at How Ocean Waves and Sea Ice Interact, Phil. Trans. R. Soc. A., 376, 20170 342, https://doi.org/10.1098/rsta.2017.0342, 2018.

Stopa, J. E., Sutherland, P., and Ardhuin, F.: Strong and highly variable push of ocean waves on Southern Ocean sea ice, Proceedings of the National Academy of Sciences, 115, 5861–5865, https://doi.org/10.1073/pnas.1802011115, 2018.

https://doi.org/10.5194/egusphere-2022-842
Preprint. Discussion started: 12 September 2022

Thomson, J.: Wave propagation in the Marginal Ice Zone: connections and feedbacks within the air-ice-ocean system, Phil Trans R Soc A, 2022.

Thomson, J., Hošeková, L., Meylan, M. H., Kohout, A. L., and Kumar, N.: Spurious Rollover of Wave Attenuation Rates in Sea Ice Caused by Noise in Field Measurements, J. Geophys. Res. Oceans, 126, https://doi.org/10.1029/2020JC016606, 2021.

Toba, Y.: Local Balance in the Air-Sea Boundary Processes, Journal of the Oceanographical Society of Japan, 29, 209–220, https://doi.org/10.1007/BF02108528, 1973.

Tolman, H. L.: User Manual and System Documentation of WAVEWATCH III TM Version 3.14, Tech. Note MMAB Contrib., 276, 220, 2009.

Tsallis, C. and Stariolo, D. A.: Generalized Simulated Annealing, Physica A: Statistical Mechanics and its Applications, 233, 395–406, https://doi.org/10.1016/S0378-4371(96)00271-3, 1996.

Villas Bôas, A. B. and Young, W. R.: Directional Diffusion of Surface Gravity Wave Action by Ocean Macroturbulence, J. Fluid Mech., 890, https://doi.org/10.1017/jfm.2020.116, 2020.

Wunsch, C.: The Ocean Circulation Inverse Problem, Cambridge University Press, Cambridge, https://doi.org/10.1017/CBO9780511629570, 1996.

Yu, Y., Sandwell, D. T., Gille, S. T., and Villas Bôas, A. B.: Assessment of ICESat-2 for the Recovery of Ocean Topography, Geophysical Journal International, 226, 456–467, https://doi.org/10.1093/gji/ggab084, 2021.